UC Berkeley

Title

Room-Temperature Ferroelectric Epitaxial Nanowire Arrays with Photoluminescence

Permalink

Journal

ISSN

Authors

Le, Han KD
Zhang, Ye
Behera, Piush
et al.

Publication Date

DOI

Room-temperature ferroelectric epitaxial nanowire arrays with photoluminescence

Han K. D. Le[1,2,‡], Ye Zhang[1,2,‡], Piush Behera[2,3], Arturas Vailionis[4,5], Amelyn Phang[3],

Rafaela M. Brinn[1], Peidong Yang[1,2,3,6,7,*]

[1]Department of Chemistry, University of California, Berkeley, CA 94720, USA.

[2]Materials Sciences Division, Lawrence Berkeley National Laboratory, Berkeley, CA 94720, USA.

[3]Department of Materials Science and Engineering, University of California, Berkeley, CA 94720, USA.

[4]Stanford Nano Shared Facilities, Stanford University, Stanford, CA 94305, USA.

[5]Department of Physics, Kaunas University of Technology, LT-51368 Kaunas, Lithuania.

[6]Kavli Energy NanoScience Institute, Berkeley, CA 94720, USA.

[7]Lead Contact. Email: p_yang@berkeley.edu (P.Y.)

*Corresponding Author. Email: p_yang@berkeley.edu (P.Y.)

[‡]These authors contribute equally

Keywords: metal halide perovskites, nanowire, epitaxial growth, optical properties, ferroelectric

Abstract: The development of large-scale, high-quality ferroelectric semiconductor nanowire arrays with interesting light-emitting properties can address limitations in traditional wide-bandgap ferroelectrics, thus serving as building blocks for innovative device architectures and next-generation high-density optoelectronics. Here, we investigate the optical properties of ferroelectric $CsGeX_3$ (X = Br, I) halide perovskite nanowires that are epitaxially grown on muscovite mica substrates by vapor phase deposition. Detailed structural characterizations reveal an incommensurate heteroepitaxial relationship with the mica substrate. Furthermore, photoluminescence that can be tuned from yellow-green to red emissions by varying the halide composition demonstrates that these nanowire networks can serve as platforms for future optoelectronic applications. In addition, the room-temperature ferroelectricity and ferroelectric domain structures of these nanowires are characterized using second harmonic generation (SHG) polarimetry. The combination of room-temperature ferroelectricity with photoluminescence in these nanowire arrays unlocks new avenues for designing novel multifunctional materials.

Perovskites have emerged as a compelling class of material candidates that exhibit versatile applications in electronics, photonics and optoelectronics.[1–4] One of their appeals lies in their high tunability and ability to realize the coexistence of two or more crucial functionalities within a single perovskite material.[5,6] Ferroelectricity, wherein the material exhibits a spontaneous electric polarization that is tunable by external electric fields, is one such important functionality and has long garnered tremendous interest for nanoelectronics and non-volatile memory devices applications.[7–11] Conventional ferroelectrics, including the perovskite oxides, are typically insulators with low carrier mobility, wide band gaps (3-5 eV) and no luminescence, thus limiting

their applications in various optoelectronic technologies.[12–14] Therefore, the prospect of designing a material capable of serving as both a ferroelectrics and a semiconductor with photoluminescence (PL) and unique optical properties can overcome the inherent constraints of traditional ferroelectrics and hold promise for advancing multifunctional nanodevice applications, such as electric field control of luminescence properties and contactless optical reading of the ferroelectric state.[15]

Among the perovskites, $CsGeX_3$ (X = Cl, Br, I) draws special attention as it is the only class of inorganic halide perovskites with a non-centrosymmetric crystal structure,[16,17] giving rise to ferroelectric properties first experimentally evidenced in our prior report.[18] The ferroelectricity of $CsGeX_3$ is attributed to the stereochemical activity of the $4s^2$ lone pair in Ge(II), thus promoting atomic displacement of the metal cation in the $<111>_{pc}$ (pc: pseudo-cubic) direction to form electric dipoles and breaking the centrosymmetry of the crystal structure. Furthermore, $CsGeX_3$ exhibits suitable bandgaps in the visible region (1.6 to 3.3 eV),[18] setting it apart from the extensively studied wide-bandgap insulating oxide ferroelectrics. Thus, combining ferroelectricity with visible light-absorbing and light-emitting properties of a photoactive semiconductor material creates opportunities to realize additional functionalities, with light utilized to harness unconventional physical phenomena. In addition, the ability to design ferroelectric semiconductors in low-dimensional forms can further introduce unique light-matter and electronic interactions,[19–22] thereby facilitating the crucial development of cutting-edge next-generation microelectronics and novel device architectures.[19,22–26] Particularly, ferroelectric

3

semiconductor nanowires have the potential to unlock a wide range of applications in areas such as data storage memories,[27,28] nanoscale photonics,[29] and energy harvesting devices.[30]

In this work, we investigate the successful large-scale epitaxial growth of single-crystalline $CsGeX_3$ (X = Br, I) perovskite one-dimensional nanowires on muscovite mica substrates. The nanowire arrays exhibit precise alignment along the six isoperiodic directions of the mica substrates. The crystallographic orientation and epitaxial relationship of the nanowires with the mica substrate are characterized. We also demonstrate their optical capabilities and potential as a semiconductor for optoelectronic devices by showcasing yellow-green and red emission for $CsGeBr_3$ and $CsGeI_3$ nanowires, respectively. Second harmonic generation (SHG) polarimetry is further used as an indirect probe of the room-temperature ferroelectricity in these nanowires. This study represents a significant strive towards large-scale preparation of well-aligned ferroelectric semiconductor nanowire arrays that are multifunctional and highly desirable for next-generation high-density optoelectronic devices and nanoelectronics.

The epitaxial growth of $CsGeX_3$ (X = Br, I) nanowires on muscovite mica was carried out via a one-step chemical vapor transport (CVT) process (see Supplementary Methods for more details regarding the experimental growth setup and conditions). Energy-dispersive X-ray spectroscopic (EDX) measurements on these epitaxial nanowires confirmed the atomic ratio of Cs:Ge:X (X = Br, I) to be approximately 1:1:3 (Figures S1 and S2). Scanning electron microscopy (SEM) and atomic force microscopy (AFM) images show that these nanowires have an equilateral triangular cross-section (Figures 1A and 1B). The nanowires have large aspect

4

ratios, with widths ranging from hundreds of nanometers to several microns and lengths from hundreds of microns to millimeters (Figures S3 and S4). It is noteworthy that the nanowires exhibit strong alignment in their growth directions, revealing a distinct six-fold symmetry that is evident from the consistent 60° or 120° angles between pairs of interconnected wires. The aligned growth directions of these nanowire networks suggest a strong matching with the pseudo-hexagonal six-fold symmetry of the mica (001) surface. Figure 1C displays the symmetrical X-ray diffraction pattern of $CsGeBr_3$ nanowires grown on muscovite mica. The mica substrate can be indexed to a monoclinic lattice and exhibits equally spaced diffraction peaks at 17.9°, 26.9°, 36.1°, and 45.5°, which corresponds to the exposed (00l) planes (a = 5.211 Å, b = 9.040 Å, c = 20.021 Å, $\alpha = \gamma$ = 90°, β = 95.76°). Meanwhile, the $CsGeBr_3$ nanowires display prominent diffraction peaks at 22.06°, 22.54°, 44.99°, and 46.03°, corresponding to the (110), (10$\bar{1}$), (220), and (20$\bar{2}$) planes of the rhombohedral $CsGeBr_3$, respectively (space group: $R3m$, $a = b = c$ = 5.635 Å, $\alpha = \beta = \gamma$ = 88.74°). The dominance of these peaks suggest that the $[110]_{rh}$, or equivalently, the $[110]_{pc}$ direction of the nanowires is the out-of-plane direction that is perpendicular to the mica (001) plane. Raman spectra of $CsGeBr_3$ nanowires grown on mica exhibit distinct peaks at 91 cm^{-1}, 138 cm^{-1}, 163 cm^{-1}, and 210 cm^{-1} which respectively correspond to the $A_{1 \, (TO+LO)}$, E, $A_{1 \, (TO)}$, and $A_{1 \, (LO)}$ vibrational modes of the $3m$ symmetry reported in previous studies,[31] indicating that the epitaxial nanowires still maintain a local non-centrosymmetric unit cell (Figure S5).
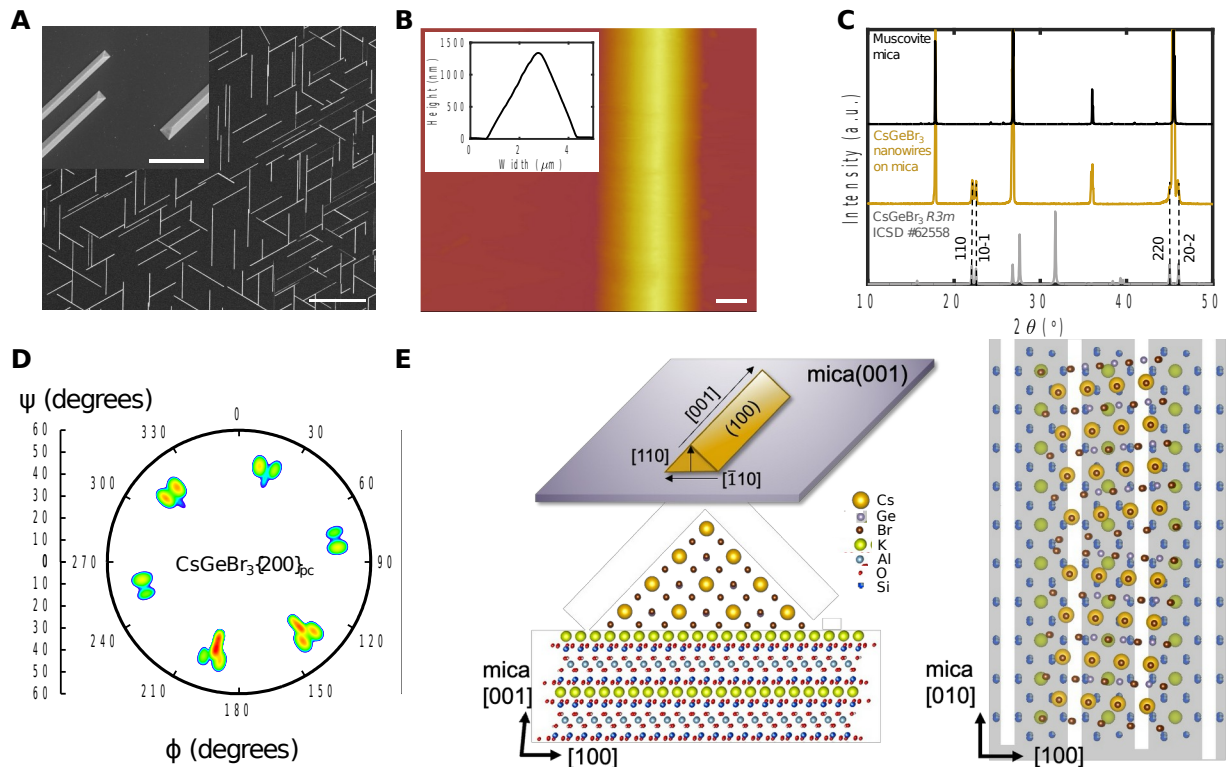
5

Figure 1. Characterization of CsGeBr$_3$ nanowires epitaxially grown on muscovite mica substrate. (A) SEM images of CsGeBr$_3$ nanowires grown on mica. Scale bar: 100 μm. Inset scale bar: 20 μm. **(B)** Representative AFM image and height profile (inset) of an individual CsGeBr$_3$ nanowire. Scale bar: 1 μm. **(C)** Symmetrical X-ray diffraction pattern of a region of CsGeBr$_3$ nanowires grown on muscovite mica (yellow, middle), and muscovite mica (black, top). Bottom gray graph represents the reference pattern for CsGeBr$_3$ *R3m* structure (Inorganic Crystal Structure Database #62558). **(D)** X-ray CsGeBr$_3${200}$_{pc}$ (pc: pseudo-cubic) pole figure revealing epitaxial relationship between mica and CsGeBr$_3$ nanowires. **(E)** Schematic illustration of the CsGeBr$_3$ nanowire growth orientation and the epitaxial relationship on mica. Bottom left inset represents the side view of the reconstructed atomic arrangement of the CsGeBr$_3$ nanowire (yellow: Cs,

6

purple: Ge, brown: Br) on the (001) plane of mica (green: K, dark blue: Si, light blue: Al, red: O, pink: H). Right inset represents the top view of such arrangement and the proposed incommensurate epitaxial relationship derived from the pole figure in Figure 1D (Al, O, H atoms hidden from view).

The van der Waals epitaxial growth of $CsPbX_3$ halide perovskites nanostructures on mica has been well studied, [20,25,32–37] but to date there is currently no in-depth report characterizing the epitaxial growth of $CsGeX_3$. This mode of epitaxy is facilitated by the unique properties of the mica substrate, whose chemically inert nature alleviates the need for strict lattice matching conditions.[25,32–36] Muscovite mica is a layered structure consisted of positively charged K^+ ions inserted between adjacent negatively charged tetrahedral aluminosilicate sheets. These neighboring layers are connected by weak van der Waals forces, which enables an easy cleavage parallel to the {001} basal plane and results in an atomically flat surface devoid of dangling bonds.[32,33,38] To simplify the communication of our results, we opted to use pseudo-cubic (pc) notation ($a = b = c = 5.635$ Å, $\alpha = \beta = \gamma = 90°$) of $CsGeBr_3$ hereafter, instead of the rhombohedral unit cell representation. To determine the crystallographic orientation of the $CsGeBr_3$ nanowires in relation to the muscovite mica substrate, two X-ray pole figures were obtained at $2\theta = 32.06°$ and $31.86°$ for mica {116} and $CsGeBr_3$ {200}$_{pc}$, respectively (Figure 1D). In these measurements, the diffracted intensity of a Bragg reflection was obtained as a function of the tilt angle, ψ, and the rotation angle, φ, with respect to the sample surface normal while the θ-2θ angles were fixed. As evident from the presence of six equidistant poles at a tilt angle $\psi = 34.65°$ and $\Delta\varphi = 60°$, mica exhibits three equivalent twin domains that rotate $60°$

relatively from each other, wherein one domain produces two {116} poles separated by 180°

(e.g.: one domain producing two poles at φ = 17° and φ = 197°). Similarly, we also observed 12

{200}$_{pc}$ CsGeBr$_3$ poles at a tilt angle ψ = 45.62°. CsGeBr$_3$ can align in two symmetrically

equivalent orientations rotated by 90° on mica, which would result in a set of two poles separated

at an azimuthal interval of 180°. Therefore, we have three symmetrically equivalent sets of

CsGeBr$_3$ twin domains separated at an azimuthal interval of 60°, each set aligning with each of

the three twin domains from mica. Each 60° CsGeBr$_3$ twin domain is further split into two

symmetrically equivalent CsGeBr$_3$ orientations that are rotated by 10° on the mica substrate. A

schematic illustration for the twin domain configurations of both the nanowires and mica as well

as their detailed alignment can be found in Figure S6. From the pole figures, the nanowire

growth axis was determined to be along the [001]$_{pc}$ direction. We proposed an incommensurate

epitaxial relationship between the as-grown CsGeBr$_3$ nanowires and the mica substrate:

CsGeBr$_3$[001]$_{pc}$ // mica[100] and CsGeBr$_3$[1$\bar{1}$0]$_{pc}$ // mica[010] along the two perpendicular in-

plane directions (Figure 1E). In this model, one periodicity of CsGeBr$_3$[001]$_{pc}$ approximately

matches with one periodicity of mica[100], with a lattice mismatch factor f of 8.1% (

$$f = \frac{d_{overlayer}}{d_{substrate}} - 1$$), whereas 8 periodicities of CsGeBr$_3$[1$\bar{1}$0]$_{pc}$ approximately matches with 7

periodicities of mica[010], with an f value of 0.74%. While van der Waals epitaxy prevails as a

more typical description in literature for muscovite mica substrates, [20,25,32–37] the contribution of

ionic interaction also emerges as significant, especially at the interface with an ionic material like

metal halide perovskites.[34] In the case of CsPbBr$_3$, an analogous halide perovskite, a strong ionic

interfacial interaction between the K$^+$ layer from mica and the I$^-$ from the PbI$_2$ layer of (001)$_{pc}$

oriented CsPbBr$_3$ nanoplates has been predicted from DFT simulations.[34] We anticipate a similar

8

atomic interaction at the interface in this work (Figure 1E, bottom left inset). As demonstrated by Franceschi *et al.*,[58] mica easily cleaves at the K^+ layers, where the surface K^+ ions are divided in half on each surface and arranged in straight alternating rows or zigzag rows with short-ranged order (Figure 1E, right inset, showing a particular configuration of such K^+ ion arrangement at the cleaved mica interface). Therefore, a strong ionic interaction at the perovskite-substrate interface is also likely between the K^+ layer from mica and the Br^- termination of the $CsGeBr_3$ nanowires.
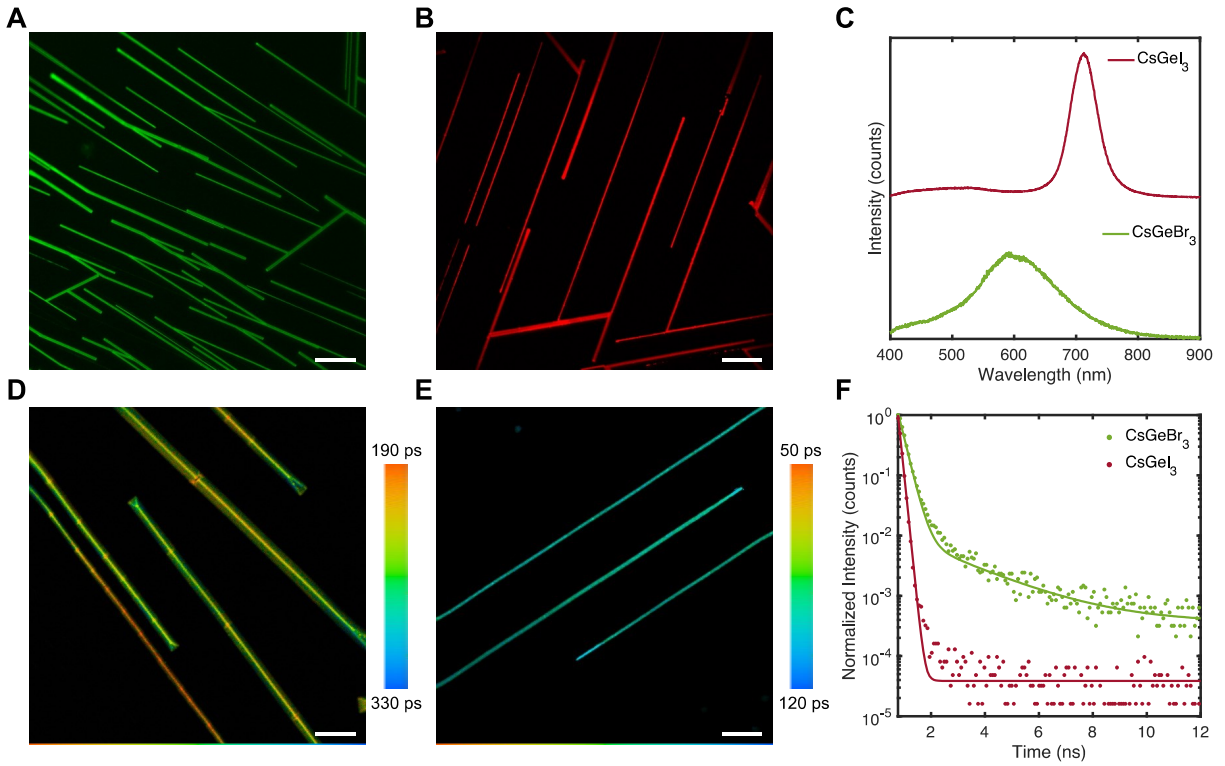

Figure 2. Optical characterizations of $CsGeX_3$ (X = Br, I) nanowires grown on muscovite mica. (A) Confocal photoluminescence (PL) image of $CsGeBr_3$ nanowires (λ_{ex}= 405 nm, emission channel: 450 nm - 650 nm). Scale bar: 50 μm. **(B)** Confocal PL image of $CsGeI_3$

nanowires (λ_{ex}= 405 nm, emission channel: 660 nm - 730 nm). Scale bar: 50 μm. **(C)** Steady-state PL spectra (λ_{ex}= 375 nm) of CsGeBr$_3$ (green, bottom) and CsGeI$_3$ (red, top) nanowires grown on mica at room temperature. **(D)** PL lifetime image of CsGeBr$_3$ nanowires (λ_{ex}= 488 nm, emission channel: 530 nm - 630 nm). Scale bar: 25 μm. **(E)** PL lifetime image of CsGeI$_3$ nanowires (λ_{ex}= 488 nm, emission channel: 680 nm - 720 nm). Scale bar: 25 μm. **(F)** Time-resolved PL decay curves (dots) and their monoexponential decay fitting curves (solid lines) for CsGeBr$_3$ nanowires (green) and CsGeI$_3$ nanowires (red).

The optical properties of metal halide perovskites have been extensively studied owing to their versatile applications including solar cells, lighting and displays.[39–42] One current research avenue is to find alternative lead-free halide perovskite materials that are non-toxic yet capable of demonstrating exceptional optical properties. In this context, we examined the room-temperature optical emission behaviors of the as-grown CsGeX$_3$ nanowires on mica. Under excitation of a 405-nm continuous-wave laser, uniform emissions along both CsGeBr$_3$ and CsGeI$_3$ nanowires were observed, as shown by the confocal PL images in Figure 2A and 2B. Figure 2C shows the normalized PL spectra of a region of CsGeBr$_3$ (top) and CsGeI$_3$ nanowires (bottom), respectively. Broad wavelength tunability can be observed by replacement of the halide anion. The CsGeBr$_3$ nanowires exhibit a broad emission band centered around 591 nm (2.10 eV) with full-width half-maximum (FWHM) of approximately 120 nm, while the CsGeI$_3$ nanowires show emission at 712 nm (1.74 eV) with FWHM of 50 nm. These emission peaks are directly related to the minimum band gap energy of both CsGeBr$_3$ and CsGeI$_3$ previously reported,[18,43] and are also comparable with PL spectra taken by us on bulk CsGeX$_3$ crystals (Figure S7) and reported

elsewhere.[43,44] To date, the number of experimental reports on Ge-containing halide perovskites are limited,[44,45] and the optical properties of CsGeX$_3$ nanowires are unexplored. The broad PL emissions observed in our CsGeBr$_3$ nanowires and bulk crystals are common in Ge-based halides,[44,46–49] thus making them promising candidates for broadband emitting materials. The stereochemically active ns^2 lone pair in metal cations has been hypothesized to play an important role in the broadband emission often observed in halide perovskites with off-centering distorted octahedra.[50–53] As the lone pair activity increases, the inorganic lattice becomes softer and more vulnerable to interact with excitons.[50] This would facilitate strong electron-phonon coupling that leads to exciton self-trapping and the formation of broadband emission.[50,51] The room-temperature PL emissions for CsGeI$_3$ nanowires is less broad and more representative of bandgap emission. We also used fluorescence lifetime mapping to probe the carrier dynamics in the nanowires (Figures 2D and 2E). Quantitative fitting to the PL decay curves resulted in a carrier recombination lifetime ranging from 250 ps for CsGeBr$_3$ to 105 ps for CsGeI$_3$ (Figure 2F). The lifetime on the order of picosecond timescale has been similarly observed in other vapor-phase grown perovskite nanowires,[20] and can be attributed to surface state recombination. The CsGeBr$_3$ nanowires exhibit faster lifetimes at regular intervals along the wires, likely attributed to the strain-induced defects occurring at these points. These defects—indeed fractures and cracks—arise as a way to release strain formed due to the temperature change during the cooling phase of the growth process and the large difference in the thermal expansion coefficients between the perovskite layer and the mica substrate.[36] These defects are less pronounced in CsGeI$_3$, possibly due to slight variations in the thermal expansion coefficient, the lattice "softness," and the alignment of lattice parameters with mica. PL performance in Ge-based

perovskites has been typically overlooked, since they are generally weak emitters compared to the analogous Pb-based perovskites.[43,44] The PL of $CsGeX_3$ nanowires, while detectable, falls below the detection limit of standard commercial photoluminescence quantum yield setups commonly utilized for denser samples and films; consequently, future optimization efforts would be required to viably exploit this system for practical device applications. It is worth noting that $CsGeCl_3$ nanowires, having a UV bandgap of 3.3 eV (375 nm),[18] can also be epitaxially grown on mica with our CVT method. The optical properties of these nanowires can be readily investigated with appropriate UV optics. The above optical characterizations demonstrate the optical capabilities and high crystallinity of the ultralong perovskite NWs, which aids in the realization of high-performance optoelectronic devices.
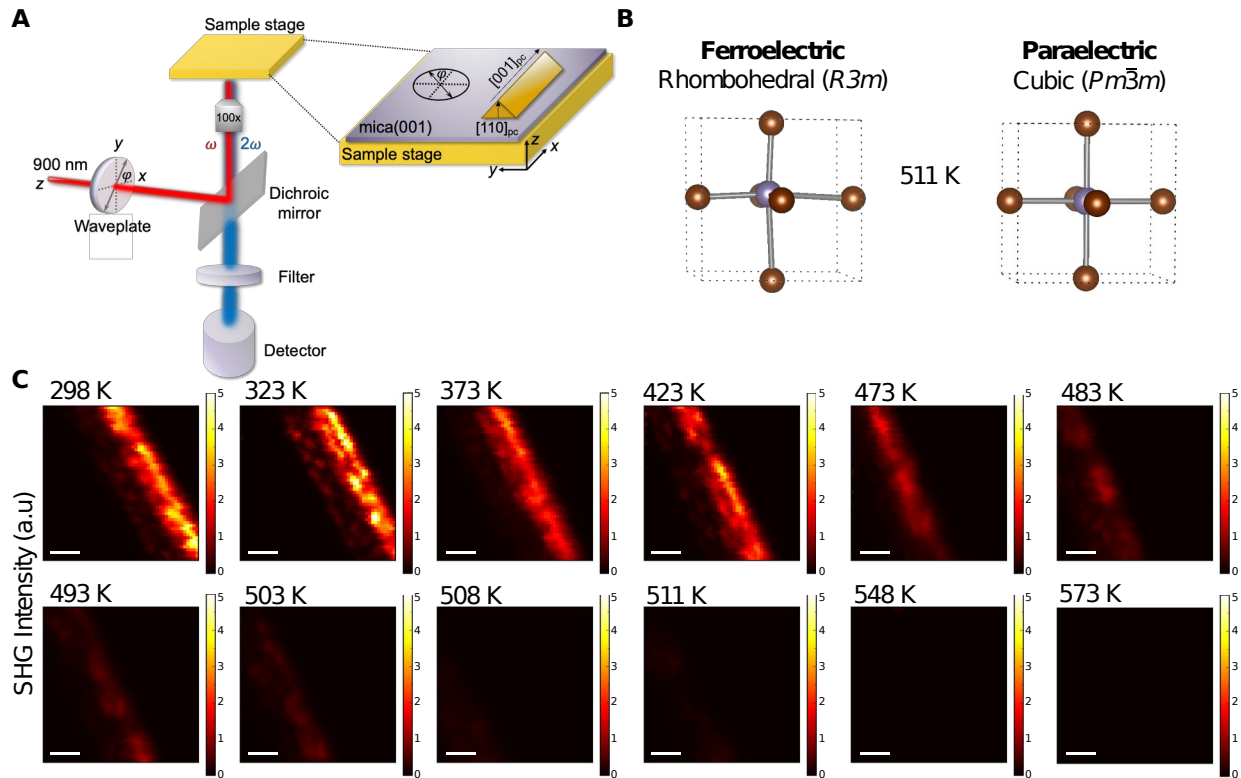

Figure 3. Temperature-dependent second harmonic generation (SHG) measurement to characterize the ferroelectric phase transition in $CsGeBr_3$ nanowires. (A) Schematic

12

diagram of the optical setup used for SHG polarimetric measurements, wherein a 900-nm fundamental beam is sent through a waveplate to control the polarizations and used to excite the frequency-doubled signal from the nanowires in a reflection geometry. We assume normal incidence of the fundamental light propagating along the *z*-axis and polarization rotating in the *xy*-plane in the lab coordinate system. The polarization angle φ is defined as the azimuthal angle of the fundamental light polarization measured from the *x*-axis. **(B)** Ferroelectric to paraelectric phase transition in $CsGeBr_3$ upon heating past 511 K. **(C)** Temperature-dependent SHG intensity maps of a representative $CsGeBr_3$ nanowire. Scale bar: 3 μm.

The integration of both photoluminescence and ferroelectricity can enrich a novel class of multifunctional materials useful for optical switching and optoelectronic applications. The ferroelectricity of $CsGeX_3$ has been known to arise from the lone pair stereochemical activity in Ge(II) that promotes the atomic displacement of the metal cation, thus causing off-centering behavior in the $<111>_{pc}$ direction and giving rise to spontaneous polarization up to 10-20 μC/cm^{-2}.[18,54] Our previous report has demonstrated the electrical switchability of ferroelectric polarizations in the $CsGeBr_3$/$CsGeI_3$ regardless of their nanoscale dimentionalities;[18] however, the ferroelectric phase transition as well as the domain structures have not been investigated in the epitaxial one-dimensional nanowire system. To

13

that end, we used optical second harmonic generation (SHG) measurements, including temperature-dependent SHG and SHG polarimetry, to further investigate the ferroelectric phase transition of $CsGeBr_3$ nanowires as well as characterize their polarization orientations. As the dominant SHG interaction mechanism exists only in materials that lack inversion symmetry, SHG is a sensitive probe of broken inversion symmetry.[55–57] As ferroelectrics, by definition, possess a spontaneous polarization ($\mathbf{P}_s$) within their crystal structure, and hence lack inversion symmetry, SHG can be used as a non-invasive nonlinear optical approach to probe ferroelectricity, including imaging the ferroelectric microdomain structures and measuring phase transitions.[55] The experimental setup of SHG is schematically shown in Figure 3A, where the sample orientation can be aligned with the laboratory coordinate axes and the polarization of the fundamental light can be controlled using polarizers and waveplates. $CsGeBr_3$ is expected to exhibit a low-symmetry rhombohedral phase (*R3m*) below 511 K and transform into a high-symmetry cubic phase (*Pm$\bar{3}$m*) above that temperature (Figure 3B).[18] In the low-symmetry rhombohedral phase, the Ge^{2+} ion is displaced along the body diagonal of the pseudo-cubic structure ($<111>_{pc}$),[54] thus generating spontaneous polarizations in this direction. In order to characterize the ferroelectric-paraelectric phase transition of these nanowires, we first carried out temperature-dependent SHG measurements within a single nanowire. Figure 3C shows the SHG intensity mappings when heating the nanowire at different temperatures in an inert environment. The SHG intensity decreases with temperature and gradually vanishes at a critical temperature (T_c) of approximately 511 K, signifying the onset of the ferroelectric-to-paraelectric phase transition and that the spontaneous polarization is approaching zero. Overall, the

14

mapping of the disappearance of the SHG signal also indicates that the phase transition is relatively homogeneous over a single-crystalline nanowire. Temperature-dependence SHG intensities on different nanowires can be captured (Figure S8-9), showing different phase transition profiles and slight increase in Curie temperatures (T_c) with respect to the bulk T_c in some instances. In addition, the transition is partially reversible, as indicated by the partial recovery of SHG signals upon cooling down the nanowires to room temperature (Figure S9). This observed partial recovery of ferroelectricity may potentially stem from differences in the rate of cubic-to-rhombohedral structural transition across different segments of the nanowires, and the emergence of structural disorders and defects during thermal cycling, owing to the soft lattice of halide perovskites.
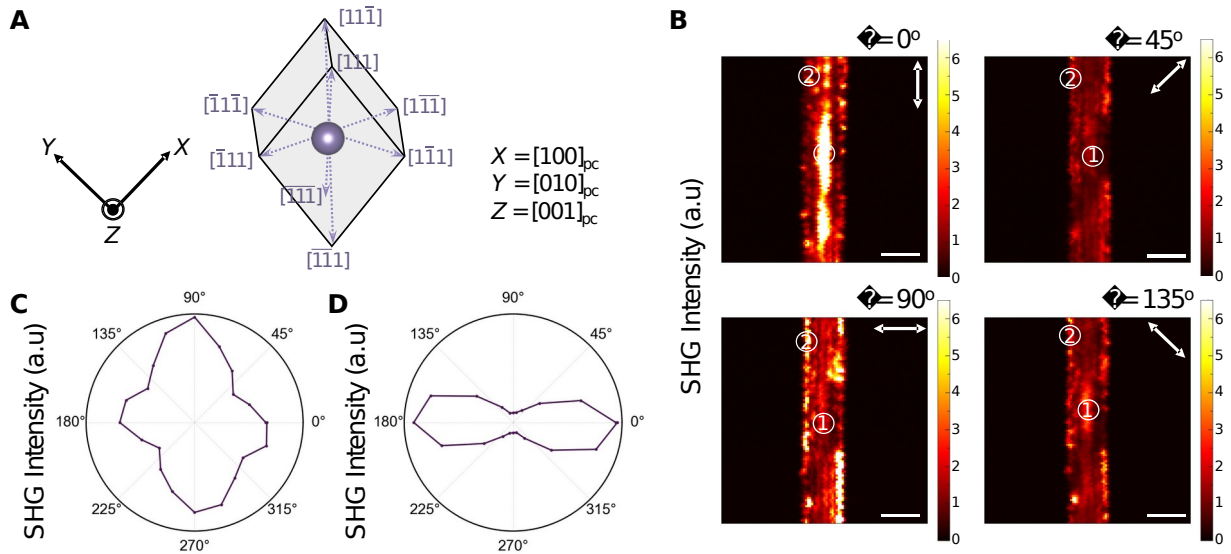
Figure 4. Polarization-dependent SHG measurement and spatial mapping of CsGeBr$_3$ nanowire. (A) Schematic representation of eight $\langle 111 \rangle_{pc}$ spontaneous polarization directions

(purple arrows) within a unit cell of $CsGeBr_3$ nanowire grown along the $[001]_{pc}$ direction. **(B)** SHG intensity maps measured at room temperature at four different polarization angles, φ = 0°, 45°, 90°, 135° (indicated double white arrows) of a representative $CsGeBr_3$ nanowire oriented such that the $[001]_{pc}$ growth axis of the nanowire is parallel to the x-axis in the laboratory coordinate system. Scale bar: 5 μm. **(C)** and **(D)** Polar plots of SHG intensity measured at room temperature as a function of incident beam polarization of the nanowire in (B) at spots 1 and 2.

Since the SHG response is highly sensitive to polarization states of the incident light with respect to electric polarization directions within ferroelectric domains, polarization-dependent SHG signals can be used to probe local domain structures and their correlated spontaneous polarization variances.[55] The $CsGeBr_3$ crystal is expected to have eight distinct ferroelectric polarizations along eight $<111>_{pc}$ directions,[18] as shown by the labeled arrows in the nanowire geometry in Figure 4A (the sample coordinate axes are defined as $X = [100]_{pc}$, $Y = [010]_{pc}$, and $Z = [001]_{pc}$ directions of the nanowire, respectively). Since the sample coordinate axes and the crystal physics axes relative to the lab frame can directly affect the measured SHG data, we orient the nanowire such that the growth axis of the nanowire (i.e, the $[001]_{pc}$ direction in the sample coordinate system) is parallel to the x-axis in the laboratory coordinate system (Figure S10). Figure 4B displays SHG intensity scanning maps for such nanowire at four fixed polarization angles, φ = 0°, 45°, 90°, and 135° (the polarization angle φ is defined as the azimuthal angle of the fundamental light polarization measured from the x-axis in the laboratory coordinate system). Under this nanowire alignment, the SHG

16

intensity contrast between domains switches for $\varphi = 90°$ and $\varphi = 180°$ and remains unchanged for $\varphi = 45°$ and $\varphi = 135°$. This result is consistent with the calculated SHG intensity at various incident polarization angles based on a second-order non-linear polarization model for our nanowire geometry and alignment (SI Methods).[18,31,55] SHG polar plots, wherein the SHG intensity at a particular spot on the nanowire is plotted as a function of incident beam polarization, are shown in Figures 4C and 4D. The polar plots show a double-lobe shape pointing either along $\varphi = 0°/180°$ or $\varphi = 90°/270°$ (i.e, along the $[001]_{pc}$ or the $[110]_{pc}$ directions of the nanowire). This indicates that the nanowires have a multi-domain structure and that the net in-plane polarizations in most of these domains are aligning with directions either parallel or perpendicular to the nanowire growth orientation, stemming from the projections of the eight $\langle 111 \rangle_{pc}$ spontaneous polarizations onto the $[001]_{pc}$ and $[110]_{pc}$ directions. A rotation of the nanowire by 90° to align its growth axis to the y-axis in the laboratory coordinate system alters the orientation of the polarization with respect to the incident fundamental light, thereby changing the relative SHG intensities of the four polarizations angles. In this nanowire geometry configuration, the SHG intensity contrast between domains also similarly switches for $\varphi = 90°$ and $\varphi = 180°$, whereas there is no observable contrast for $\varphi = 45°$ and $\varphi = 135°$ (Figure S11). Rotating the nanowire such that its growth axis is 45° or 135° from the x-axis results in the SHG intensity domains switching between $\varphi = 45°$ and $\varphi = 135°$, while remaining constant for $\varphi = 90°$ and $\varphi = 180°$ (Figure S12). These results further confirm that the in-plane components of spontaneous polarizations are either parallel or perpendicular to the nanowire growth orientation. The investigation of domain structures along with their polarization orientations in ferroelectric

17

nanowires may enable future studies and applications in nanowire-based high-density information storage and memory devices.

In summary, we investigate the large-scale epitaxial growth of $CsGeX_3$ nanowire arrays on single crystal muscovite mica substrates via vapor phase deposition. Detailed structural characterization to verify the orientation and epitaxial relationship of the nanowires with respect to the mica substrates confirmed that van der Waals epitaxial growth can be a generalized strategy to realize highly aligned halide perovskite nanostructures. The tunable yellow-green and red emission for $CsGeBr_3$ and $CsGeI_3$ nanowires demonstrate the great potential of these structures as semiconductors for optoelectronic devices. Second harmonic generation (SHG) microscopy and polarimetry are used to probe the ferroelectricity phase transition and in-plane polarization orientations of these room-temperature ferroelectric nanowires. This study shows that $CsGeX_3$ nanowires can be a promising material candidate for the advancements of light-driven multifunctional nanoscale ferroelectric devices.

Supplemental Information

The Supporting Information (PDF File) is available free of charge on the ACS Publications website.

- Experimental methods, additional experimental data (e.g., SEM/EDS, Raman spectroscopy, PL, SHG), and schematic illustrations of the nanowire alignment on the substrate and axes orientation and polarization directions in SHG measurements.

18

Author Information:

Corresponding Authors: Peidong Yang - Department of Chemistry, University of California, Berkeley, California 94720, United States; Materials Sciences Division, Lawrence Berkeley National Laboratory, Berkeley, California 94720, United States; Department of Materials Science and Engineering, University of California, Berkeley, California 94720, United States; Kavli Energy NanoScience Institute, Berkeley, California 94720, United States; Email: p_yang@berkeley.edu (P.Y.)

All authors contributed substantially to the work presented herein. H.K.D.L., Y.Z. and P.Y. conceived the study. H.K.D.L. conducted the materials synthesis, main characterizations (PXRD, SEM/EDS, AFM), optical measurements (PL, confocal laser scanning microscopy, FLIM, SHG) and data analysis. Y.Z. developed original methodologies for part of this project (material synthesis, SHG measurements). H.K.D.L, P.B. and R.B. conducted SHG polarimetry and temperature-dependent SHG measurements. H.K.D.L and A.V. conducted X-ray pole figures and analyzed the data. A.P. assisted with materials synthesis. H.K.D.L. and P.Y. wrote the manuscript. All authors contributed to writing or commented on the manuscript.

Declaration of Interests

The authors declare no competing interests.

Acknowledgments

References

(1) Rong, Y.; Hu, Y.; Mei, A.; Tan, H.; Saidaminov, M. I.; Seok, S. Il; McGehee, M. D.; Sargent, E. H.; Han, H. Challenges for Commercializing Perovskite Solar Cells. *Science* **2018**, *361* (6408), eaat8235. https://doi.org/10.1126/science.aat8235.

(2) Green, M. A.; Ho-Baillie, A.; Snaith, H. J. The Emergence of Perovskite Solar Cells. *Nat Photonics* **2014**, *8* (7), 506–514. https://doi.org/10.1038/nphoton.2014.134.

(3) Correa-Baena, J. P.; Saliba, M.; Buonassisi, T.; Grätzel, M.; Abate, A.; Tress, W.; Hagfeldt, A. Promises and Challenges of Perovskite Solar Cells. *Science* **2017**, *358* (6364), 739–744. https://doi.org/10.1126/science.aam6323.

(4) Lin, J.; Lai, M.; Dou, L.; Kley, C. S.; Chen, H.; Peng, F.; Sun, J.; Lu, D.; Hawks, S. A.; Xie, C.; Cui, F.; Alivisatos, A. P.; Limmer, D. T.; Yang, P. Thermochromic Halide Perovskite Solar Cells. *Nat Mater* **2018**, *17* (3), 261–267. https://doi.org/10.1038/s41563-017-0006-0.

(5) Spaldin, N. A.; Cheong, S. W.; Ramesh, R. Multiferroics: Past, Present, and Future. *Phys Today* **2010**, *63* (10), 38–43. https://doi.org/10.1063/1.3502547.

(6) Spaldin, N. A.; Fiebig, M. The Renaissance of Magnetoelectric Multiferroics. *Science* **2005**, *309* (5733), 391–392. https://doi.org/10.1126/science.1113357.

(7) Martin, L. W.; Rappe, A. M. Thin-Film Ferroelectric Materials and Their Applications. *Nature Reviews Materials* **2017**, *2*, 16087. https://doi.org/10.1038/natrevmats.2016.87.

(8) Scott, J. F. *Applications of Modern Ferroelectrics*. *Science* **2007**, *315* (5814), 954–959. https://doi.org/10.1126/science.1129564.

(9) Catalan, G.; Seidel, J.; Ramesh, R.; Scott, J. F. Domain Wall Nanoelectronics. *Rev Mod Phys* **2012**, *84* (1), 119–156. https://doi.org/10.1103/RevModPhys.84.119.

(10)   Yang, S. Y.; Seidel, J.; Byrnes, S. J.; Shafer, P.; Yang, C. H.; Rossell, M. D.; Yu, P.; Chu, Y. H.; Scott, J. F.; Ager, J. W.; Martin, L. W.; Ramesh, R. Above-Bandgap Voltages from Ferroelectric Photovoltaic Devices. *Nat Nanotechnol* **2010**, *5* (2), 143–147. https://doi.org/10.1038/nnano.2009.451.

(11)   Fernandez, A.; Acharya, M.; Lee, H. G.; Schimpf, J.; Jiang, Y.; Lou, D.; Tian, Z.; Martin, L. W. Thin-Film Ferroelectrics. *Advanced Materials* **2022**, *34*, 2108841. https://doi.org/10.1002/adma.202108841.

(12)   Grinberg, I.; West, D. V.; Torres, M.; Gou, G.; Stein, D. M.; Wu, L.; Chen, G.; Gallo, E. M.; Akbashev, A. R.; Davies, P. K.; Spanier, J. E.; Rappe, A. M. Perovskite Oxides for Visible-Light-Absorbing Ferroelectric and Photovoltaic Materials. *Nature* **2013**, *503* (7477), 509–512. https://doi.org/10.1038/nature12622.

(13)   Benedek, N. A.; Fennie, C. J. Why Are There so Few Perovskite Ferroelectrics? *Journal of Physical Chemistry C* **2013**, *117* (26), 13339–13349. https://doi.org/10.1021/jp402046t.

(14)   Kan, D.; Terashima, T.; Kanda, R.; Masuno, A.; Tanaka, K.; Chu, S.; Kan, H.; Ishizumi, A.; Kanemitsu, Y.; Shimakawa, Y.; Takano, M. Blue-Light Emission at Room Temperature from Ar+-Irradiated $SrTiO_3$. *Nat Mater* **2005**, *4* (11), 816–819. https://doi.org/10.1038/nmat1498.

(15)   Handa, T.; Hashimoto, R.; Nakamura, T.; Wakamiya, A.; Kanemitsu, Y. Metal-Free Ferroelectric Halide Perovskite Exhibits Visible Photoluminescence Correlated with Local Ferroelectricity. *Sci Adv* **2022**, *8* (25), eabo1621. https://doi.org/10.1126/sciadv.abo162.

(16)   Christensen, A. N.; Rasmussen, S. E. A Ferroelectric Chloride of Perovskite Type: Crystal Structures of $CsGeCl_3$. *Acta Chem Scand* **1965**, *19*, 421–428.

(17)   Thiele, G.; Rotter, H. W.; Schmidt, K. D. Kristallstrukturen Und Phasentransformationen von Caesiumtrihalogenogermanaten(II) CsGeX3 (X = Cl, Br, I). *ZAAC - Journal of Inorganic and General Chemistry* **1987**, *545* (2), 148–156. https://doi.org/10.1002/zaac.19875450217.

(18)   Zhang, Y.; Parsonnet, E.; Fernandez, A.; Griffin, S. M.; Huyan, H.; Lin, C.-K.; Lei, T.; Jin, J.; Barnard, E. S.; Raja, A.; Behera, P.; Pan, X.; Ramesh, R.; Yang, P. Ferroelectricity in a Semiconducting All-Inorganic Halide Perovskite. *Sci Adv* **2022**, *8* (6), eabj5881. https://doi.org/10.1126/sciadv.abj5881.

(19)   Eaton, S. W.; Fu, A.; Wong, A. B.; Ning, C. Z.; Yang, P. Semiconductor Nanowire Lasers. *Nature Reviews Materials* **2016**, *1*, 16028. https://doi.org/10.1038/natrevmats.2016.28.

(20)   Lu, D.; Zhang, Y.; Lai, M.; Lee, A.; Xie, C.; Lin, J.; Lei, T.; Lin, Z.; Kley, C. S.; Huang, J.; Rabani, E.; Yang, P. Giant Light-Emission Enhancement in Lead Halide Perovskites by Surface Oxygen Passivation. *Nano Lett* **2018**, *18* (11), 6967–6973. https://doi.org/10.1021/acs.nanolett.8b02887.

(21)   Agarwal, R.; Barrelet, C. J.; Lieber, C. M. Lasing in Single Cadmium Sulfide Nanowire Optical Cavities. *Nano Lett* **2005**, *5* (5), 917–920. https://doi.org/10.1021/nl050440u.

(22)   Yan, R.; Gargas, D.; Yang, P. Nanowire Photonics. *Nature Photonics* **2009**, *3*, 569–576. https://doi.org/10.1038/nphoton.2009.184.

(23)   Lin, C. K.; Zhang, Y.; Gao, M.; Lin, J. A.; Le, H. K. D.; Lin, Z.; Yang, P. Controlling the Phase Transition in CsPbI3 Nanowires. *Nano Lett* **2022**, *22* (6), 2437–2443. https://doi.org/10.1021/acs.nanolett.2c00170.

(24) Chen, J.; Fu, Y.; Samad, L.; Dang, L.; Zhao, Y.; Shen, S.; Guo, L.; Jin, S. Vapor-Phase Epitaxial Growth of Aligned Nanowire Networks of Cesium Lead Halide Perovskites (CsPbX3, X = Cl, Br, I). *Nano Lett* **2020**, *17* (1), 460–466. https://doi.org/10.1021/acs.nanolett.6b04450.

(25) Wang, Y.; Sun, X.; Shivanna, R.; Yang, Y.; Chen, Z.; Guo, Y.; Wang, G. C.; Wertz, E.; Deschler, F.; Cai, Z.; Zhou, H.; Lu, T. M.; Shi, J. Photon Transport in One-Dimensional Incommensurately Epitaxial CsPbX3 Arrays. *Nano Lett* **2016**, *16* (12), 7974–7981. https://doi.org/10.1021/acs.nanolett.6b04297.

(26) Yang, P. Semiconductor Nanowire, What's next II? *Next Materials* **2023**, *1* (2), 100014. https://doi.org/10.1016/j.nxmate.2023.100014.

(27) Liao, L.; Fan, H. J.; Yan, B.; Zhang, Z.; Chen, L. L.; Li, B. S.; Xing, G. Z.; Shen, Z. X.; Wu, T.; Sun, X. W.; Wang, J.; Yu, T. Ferroelectric Transistors with Nanowire Channel: Toward Nonvolatile Memory Applications. *ACS Nano* **2009**, *3* (3), 700–706. https://doi.org/10.1021/nn800808s.

(28) Yun, W. S.; Urban, J. J.; Gu, Q.; Park, H. Ferroelectric Properties of Individual Barium Titanate Nanowires Investigated by Scanned Probe Microscopy. *Nano Lett* **2002**, *2* (5), 447–450. https://doi.org/10.1021/nl015702g.

(29) Nakayama, Y.; Pauzauskie, P. J.; Radenovic, A.; Onorato, R. M.; Saykally, R. J.; Liphardt, J.; Yang, P. Tunable Nanowire Nonlinear Optical Probe. *Nature* **2007**, *447* (7148), 1098–1101. https://doi.org/10.1038/nature05921.

(30) Wang, Z.; Hu, J.; Suryavanshi, A. P.; Yum, K.; Yu, M. F. Voltage Generation from Individual BaTiO 3 Nanowires under Periodic Tensile Mechanical Load. *Nano Lett* **2007**, *7* (10), 2966–2969. https://doi.org/10.1021/nl070814e.

24

(31) Huang, L. Y.; Lambrecht, W. R. L. Vibrational Spectra and Nonlinear Optical Coefficients of Rhombohedral CsGeX3 Halide Compounds with X= I, Br, Cl. *Phys Rev B* **2016**, *94*, 115202. https://doi.org/10.1103/PhysRevB.94.115202.

(32) Wang, Y.; Jia, C.; Fan, Z.; Lin, Z.; Lee, S. J.; Atallah, T. L.; Caram, J. R.; Huang, Y.; Duan, X. Large-Area Synthesis and Patterning of All-Inorganic Lead Halide Perovskite Thin Films and Heterostructures. *Nano Lett* **2021**, *21* (3), 1454–1460. https://doi.org/10.1021/acs.nanolett.0c04594.

(33) Chen, J.; Fu, Y.; Samad, L.; Dang, L.; Zhao, Y.; Shen, S.; Guo, L.; Jin, S. Vapor-Phase Epitaxial Growth of Aligned Nanowire Networks of Cesium Lead Halide Perovskites (CsPbX3, X = Cl, Br, I). *Nano Lett* **2020**, *17* (1), 460–466. https://doi.org/10.1021/acs.nanolett.6b04450.

(34) Wang, Y.; Gao, L.; Yang, Y.; Xiang, Y.; Chen, Z.; Dong, Y.; Zhou, H.; Cai, Z.; Wang, G. C.; Shi, J. Nontrivial Strength of van Der Waals Epitaxial Interaction in Soft Perovskites. *Phys Rev Mater* **2018**, *2*, 076002. https://doi.org/10.1103/PhysRevMaterials.2.076002.

(35) Zhang, Q.; Su, R.; Liu, X.; Xing, J.; Sum, T. C.; Xiong, Q. High-Quality Whispering-Gallery-Mode Lasing from Cesium Lead Halide Perovskite Nanoplatelets. *Adv Funct Mater* **2016**, *26* (34), 6238–6245. https://doi.org/10.1002/adfm.201601690.

(36) Le, H. K. D.; Lin, C. K.; Jin, J.; Zhang, Y.; Lin, Z.; Vailionis, A.; Tamura, N.; Yang, P. Quantification of Strain and Its Impact on the Phase Stabilization of All-Inorganic Cesium Lead Iodide Perovskites. *Matter* **2023**, *6* (7), 2368–2382. https://doi.org/10.1016/j.matt.2023.05.027.

(37) Zhang, Y.; Lu, D.; Gao, M.; Lai, M.; Lin, J.; Lei, T.; Lin, Z.; Quan, L. N.; Yang, P. Quantitative Imaging of Anion Exchange Kinetics in Halide Perovskites. *Proc Natl Acad Sci* **2019**, *116* (26), 12648–12653. https://doi.org/10.1073/pnas.1903448116.

(38) Wang, L.; King, I.; Chen, P.; Bates, M.; Lunt, R. R. Epitaxial and Quasiepitaxial Growth of Halide Perovskites: New Routes to High End Optoelectronics. *APL Mater* **2020**, *8*, 100904. https://doi.org/10.1063/5.0017172.

(39) Lin, Z.; Folgueras, M. C.; Le, H. K. D.; Gao, M.; Yang, P. Laser-Accelerated Phase Transformation in Cesium Lead Iodide Perovskite. *Matter* **2022**, *5* (5), 1455–1465. https://doi.org/10.1016/j.matt.2022.04.002.

(40) Gao, M.; Zhang, Y.; Lin, Z.; Jin, J.; Folgueras, M. C.; Yang, P. The Making of a Reconfigurable Semiconductor with a Soft Ionic Lattice. *Matter* **2021**, *4* (12), 3874–3896. https://doi.org/10.1016/j.matt.2021.09.023.

(41) Liu, W.; Lin, Q.; Li, H.; Wu, K.; Robel, I.; Pietryga, J. M.; Klimov, V. I. Mn2+-Doped Lead Halide Perovskite Nanocrystals with Dual-Color Emission Controlled by Halide Content. *J Am Chem Soc* **2016**, *138* (45), 14954–14961. https://doi.org/10.1021/jacs.6b08085.

(42) Li, X.; Cao, F.; Yu, D.; Chen, J.; Sun, Z.; Shen, Y.; Zhu, Y.; Wang, L.; Wei, Y.; Wu, Y.; Zeng, H. All Inorganic Halide Perovskites Nanosystem: Synthesis, Structural Features, Optical Properties and Optoelectronic Applications. *Small* **2017**, *13* (9), 1–24. https://doi.org/10.1002/smll.201603996.

(43) Zeng, H.; Yao, F.; Li, R.; Song, D.; Li, Y.; Lin, Q.; Xie, R. J. Thermal Evaporation of Lead-Free Inorganic Perovskite CsGeI3 for Photodetection. *Appl Phys Lett* **2022**, *121*, 101101. https://doi.org/10.1063/5.0108781.

(44) Liu, Y.; Gong, Y. P.; Geng, S.; Feng, M. L.; Manidaki, D.; Deng, Z.; Stoumpos, C. C.; Canepa, P.; Xiao, Z.; Zhang, W. X.; Mao, L. Hybrid Germanium Bromide Perovskites with Tunable

Second Harmonic Generation. *Angewandte Chemie - International Edition* **2022**, *61* (43). https://doi.org/10.1002/anie.202208875.

(45)   Chen, L. J. Synthesis and Optical Properties of Lead-Free Cesium Germanium Halide Perovskite Quantum Rods. *RSC Adv* **2018**, *8* (33), 18396–18399. https://doi.org/10.1039/c8ra01150h.

(46)   Stoumpos, C. C.; Frazer, L.; Clark, D. J.; Kim, Y. S.; Rhim, S. H.; Freeman, A. J.; Ketterson, J. B.; Jang, J. I.; Kanatzidis, M. G. Hybrid Germanium Iodide Perovskite Semiconductors: Active Lone Pairs, Structural Distortions, Direct and Indirect Energy Gaps, and Strong Nonlinear Optical Properties. *J Am Chem Soc* **2015**, *137* (21), 6804–6819. https://doi.org/10.1021/jacs.5b01025.

(47)   Mitzi, D. B. Synthesis, Crystal Structure, and Optical and Thermal Properties of (C4H9NH3)2MI4 (M = Ge, Sn, Pb). *Chem. Mater.* **1996**, *8*, 791–800.

(48)   Cheng, P.; Wu, T.; Zhang, J.; Li, Y.; Liu, J.; Jiang, L.; Mao, X.; Lu, R. F.; Deng, W. Q.; Han, K. (C6H5C2H4NH3)2GeI4: A Layered Two-Dimensional Perovskite with Potential for Photovoltaic Applications. *Journal of Physical Chemistry Letters* **2017**, *8* (18), 4402–4406. https://doi.org/10.1021/acs.jpclett.7b01985.

(49)   Morad, V.; Shynkarenko, Y.; Yakunin, S.; Brumberg, A.; Schaller, R. D.; Kovalenko, M. V. Disphenoidal Zero-Dimensional Lead, Tin, and Germanium Halides: Highly Emissive Singlet and Triplet Self-Trapped Excitons and X-Ray Scintillation. *J Am Chem Soc* **2019**, *141* (25), 9764–9768. https://doi.org/10.1021/jacs.9b02365.

(50)   Jiang, X.; Tao, Y.; Gu, J.; Jin, L.; Li, C.; Zhang, W.; Fu, Y. Broadband Emission Originating from the Stereochemical Expression of 6s2 Lone Pairs in Two-Dimensional Lead Bromide
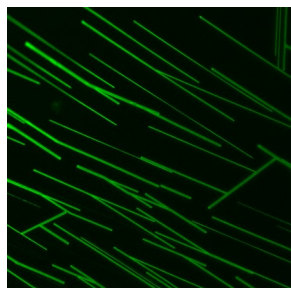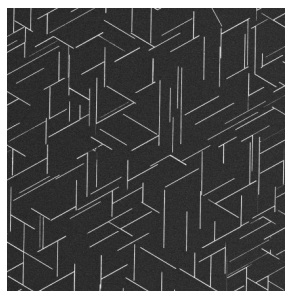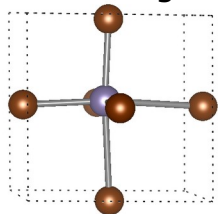
Perovskites. *Dalton Transactions* **2023**, *52* (42), 15489–15495. https://doi.org/10.1039/d3dt01627g.

(51)   Han, X. Bin; Jing, C. Q.; Zu, H. Y.; Zhang, W. Structural Descriptors to Correlate Pb Ion Displacement and Broadband Emission in 2D Halide Perovskites. *J Am Chem Soc* **2022**, *144* (40), 18595–18606. https://doi.org/10.1021/jacs.2c08364.

(52)   Lü, X.; Stoumpos, C.; Hu, Q.; Ma, X.; Zhang, D.; Guo, S.; Hoffman, J.; Bu, K.; Guo, X.; Wang, Y.; Ji, C.; Chen, H.; Xu, H.; Jia, Q.; Yang, W.; Kanatzidis, M. G.; Mao, H. K. Regulating Off-Centering Distortion Maximizes Photoluminescence in Halide Perovskites. *Natl Sci Rev* **2021**, *8* (9), nwaa288. https://doi.org/10.1093/nsr/nwaa288.

(53)   Hou, A.; Fan, L.; Xiong, Y.; Lin, J.; Liu, K.; Chen, M.; Guo, Z.; Zhao, J.; Liu, Q. Zero-Dimensional Halides with Ns2 Electron (Sb3+) Activation to Generate Broad Photoluminescence. *Inorg Chem* **2023**, *62* (31), 12501–12509. https://doi.org/10.1021/acs.inorgchem.3c01726.

(54)   Fabini, D. H.; Seshadri, R.; Kanatzidis, M. G. The Underappreciated Lone Pair in Halide Perovskites Underpins Their Unusual Properties. *MRS Bull* **2020**, *45* (6), 467–477. https://doi.org/10.1557/mrs.2020.142.

(55)   Denev, S. A.; Lummen, T. T. A.; Barnes, E.; Kumar, A.; Gopalan, V. Probing Ferroelectrics Using Optical Second Harmonic Generation. *Journal of the American Ceramic Society* **2011**, *94* (9), 2699–2727. https://doi.org/10.1111/j.1551-2916.2011.04740.x.

(56)   Gao, H.; Chen, C.; You, L.; Sun, F.; Lu, C.; Yang, S.; Zhou, G.; Chen, D.; Han, Y.; Liu, J. M. Co-Polarized Second Harmonic Generation Induced by Ferroelectric Domains and Domain Wall Arrays. *Adv Opt Mater* **2022**, *10*, 2200831. https://doi.org/10.1002/adom.202200831.

(57)   Trassin, M.; Luca, G. De; Manz, S.; Fiebig, M. Probing Ferroelectric Domain Engineering in BiFeO3 Thin Films by Second Harmonic Generation. *Advanced Materials* **2015**, *27* (33), 4871–4876. https://doi.org/10.1002/adma.201501636.

(58)   Franceschi, G.; Kocán, P.; Conti, A.; Brandstetter, S.; Balajka, J.; Sokolović, I.; Valtiner , M.; Mittendorfer, F.; Schmid, M.; Setvín, M.; Diebold, U. Resolving the intrinsic short-range ordering of K+ ions on cleaved muscovite mica. *Nature Communications* **2023**, *14*, 208. https://doi.org/10.1038/s41467-023-35872-y.

For Table of Contents Only

Ferroelectric CsGeX$_3$